





Small-scale fluctuation and scaling law of mixing in three-dimensional rotating turbulent Rayleigh-Taylor instability

Yikun Wei ¹, Yumeng Li,¹ Zhengdao Wang ^{1,*}, Hui Yang,¹ Zuchao Zhu,¹ Yuehong Qian,² and Kai H. Luo ³

¹Faculty of Mechanical Engineering and Automation, Zhejiang Sci-Tech University, 310018 Zhejiang, China

²School of Mathematical Sciences, Soochow University, 215031 Jiangsu, China

³Department of Mechanical Engineering, University College London, Torrington Place, London WC1E 7JE, United Kingdom

 (Received 25 June 2021; revised 5 December 2021; accepted 4 January 2022; published 25 January 2022)

The effect of rotation on small-scale characteristics and scaling law in the mixing zone of the three-dimensional turbulent Rayleigh-Taylor instability (RTI) is investigated by the lattice Boltzmann method at small Atwood number. The mixing zone width $h(t)$, the root mean square of small scale fluctuation, the spectra, and the structure functions are obtained to analyze the rotating effect. We mainly focus on the process of the development of plumes and discuss the physical mechanism in the mixing zone in rotating and nonrotating systems. The variation of kinetic energy spectra E_u and temperature energy spectra E_θ with the dimensionless rotation $\Omega\tau$ demonstrate the suppression effect of rotation. Two scaling laws between the mixing layer width $h(t)$ and dimensionless time t/τ are obtained at various Coriolis forces ($\sqrt{h(t)} \simeq t^{0.9}$ and $\sqrt{h(t)} \simeq t^{0.35}$). The rotation increasingly suppresses the growth of the mixing layer width $h(t)$. The velocity and temperature fluctuations are also suppressed by the rotation effect. The relation between the Nusselt number (Nu) and the Rayleigh number (Ra) indicates that the heat transfer is suppressed by the rotation effect in the rotating RT system. The width of the inertial subrange increasingly narrows with increasing $\Omega\tau$.

DOI: [10.1103/PhysRevE.105.015103](https://doi.org/10.1103/PhysRevE.105.015103)

I. INTRODUCTION

It is well known that the Rayleigh-Taylor instability (RTI) mainly occurs at the interface of the density gradient of two different fluid densities or the superior temperature gradient of one fluid [1–6]. The instability gradually develops into a fully turbulent flow with time evolution [2]. The unstable layered interfaces widely occur in nature. Mixing of fluid introduced by RTI and turbulence is characteristic of many systems [3]. The RTI of multiwavelength occurs in geology to reveal the polydiapirs evolution [4]. The RTI of flame acceleration appears in astrophysics [5]. The acceleration can make flame speed up. Moreover, the RTI brings the orogeny of the intraplate in the lithosphere beneath the Earth's mantle [6]. The RTI mixing evolution is studied by numerical and experimental works under various physical conditions [7,8]. RTI also occurs in different kinds of significant circumstances relating to the engineering processes and inertial confinement fusion. The turbulent fluctuations of small scales for RTI were widely studied over the past several decades [6,9]. Flow characteristics of small scale and increasingly larger scales occur at a transitionally chaotic state induced by the instability in RTI [10]. Chertkov *et al.* [9] proposed a theoretical model of the energy transport processes. It was found that the temporal behavior of a large-scale relation was induced by the energy balance between the buoyancy term and the temporally derivative term. Zhou *et al.* [1,7] studied the scaling behavior of small-scale turbulent properties with temporal evolution, the

thermal and kinetics dissipation properties, and scale-to-scale energy and enstrophy characteristics. Zhou *et al.* [10–13] reviewed RTI and introduced the key issues and recent research progress of RTI. Zhou *et al.* [10] argued that the small-scale properties of fully RT turbulence in the mixing process is a well-known problem in its own right. Zhou *et al.* [11,12] also reported the scaling property of the mixing layer width mainly occurs at the nonlinear mixing stage, the developing late-time phase in RTI. Meanwhile, small-scale fluctuation is affected by combustion, reaction, and rotation [6]. The fluctuations of turbulent temperature in RTI are separated by a thin active interface and eliminated by combustion. The speed and amplitude of the mixing zone are weakly influenced by the reaction in RTI [10–14].

The effect of rotation on the RTI has attracted increasing attention [6,15,16]. The rotating RTI is based on adding the Coriolis force $2\boldsymbol{\omega} \times \mathbf{u}$ ($|\boldsymbol{\omega}| = \Omega/2$) to the equation of RTI [17,18]. The stabilizing effect of the Coriolis force on the RTI was studied in previous works [15,16,19,20]. Both the linear and the weakly nonlinear stages are influenced in the perturbation evolution [20]. The Coriolis force can suppress the flow instability in rotating systems. Chandrasekhar [21] first considered the effect of rotation on RTI. Carnevale *et al.* [20] confirmed these predictions by numerical simulations. Tao *et al.* [19] also demonstrated the conclusion of the slowing-down effect on the mixing zone of RT turbulence. Baldwin *et al.* [15] further demonstrated the prediction by an experimental test. Recently, Boffetta *et al.* [6,16] argued that the heat transfer efficiency and the temperature growth rate are suppressed by the rotation in the RT mixing layer.

*dao@zstu.edu.cn

Based on the above retrospective analysis of RTI, we extended the previous works [16] by making a high-resolution numerical simulation of three-dimensional (3D) RT turbulence in this paper. Our main aim is to investigate the velocity and temperature fluctuations, the mixing layer width $h(t)$, the scaling law of small scales, and the intermittency properties with increasing $\Omega\tau$ at the same characteristic time. It is observed that the spatial intermittency fluctuations of the velocity and temperature are increasingly suppressed by the rotation. The remainder of this paper is organized as follows. Section II describes the thermal lattice Boltzmann method (LBM) in the rotating system and we introduce the basic idea of thermal LBM model with the Coriolis force. Section III demonstrates some numerical results of 3D rotating RT turbulence to illustrate the effect of rotation on the slope of mixing width $h(t)$, heat transfer efficiency, and small-scale features. Finally, a summary is presented in Sec. IV.

II. NUMERICAL METHODOLOGY

A. Hydrodynamic equations of rotating Rayleigh-Taylor turbulence

The hydrodynamic equations of rotating RTI for incompressible velocity and temperature fields are introduced in the Boussinesq approximation [6,16]

$$\frac{\partial(\mathbf{u})}{\partial t} + \mathbf{u} \cdot \nabla(\mathbf{u}) + 2\boldsymbol{\omega} \times \mathbf{u} = -\nabla(P) + \nu \nabla^2(\mathbf{u}) - \mathbf{g}\beta\theta, \quad (1)$$

$$\frac{\partial(\theta)}{\partial t} + \mathbf{u} \cdot \nabla(\theta) = \kappa \nabla^2(\theta), \quad (2)$$

where $\mathbf{u} = (u, v, w)$ is the velocity of fluid, θ is the temperature of the fluid, the plane $z = 0$ is the initial interface at $t = 0$, and $\boldsymbol{\omega} = (0, 0, \Omega/2)$ denotes the uniform rotation. The Boussinesq approximation is an efficient simplification for simulating the RTI at small Atwood number. However the RTI at large Atwood number needs to be simulated with variable density Navier-Stokes equations.

$$\mathbf{c}_i = c \begin{bmatrix} 0 & 1 & -1 & 0 & 0 & 0 & 0 & 1 & -1 & 1 & -1 & 1 & -1 & -1 & 1 & 0 & 0 & 0 & 0 \\ 0 & 0 & 0 & 1 & -1 & 0 & 0 & 1 & -1 & -1 & 1 & 0 & 0 & 0 & 0 & 1 & -1 & 1 & -1 \\ 0 & 0 & 0 & 0 & 0 & 1 & -1 & 0 & 0 & 0 & 0 & 1 & -1 & 1 & -1 & 1 & -1 & -1 & 1 \end{bmatrix},$$

$$c_s = \frac{1}{\sqrt{3}} \frac{\Delta x}{\Delta t}, \quad w_i = \begin{cases} \frac{1}{3} & i = 0, \\ \frac{1}{18} & i = 1 \sim 6, \\ \frac{1}{36} & i = 7 \sim 18. \end{cases} \quad (6)$$

The relation between the relaxation parameter ω_f and kinematic viscosity ν is

$$\nu = c_s^2 \left(\frac{1}{\omega_f} - \frac{1}{2} \right) \Delta t, \quad (7)$$

where the macroscopic density and velocity are calculated by

$$\rho = \sum_i f_i, \quad \rho \mathbf{u} = \sum_i f_i \mathbf{c}_i. \quad (8)$$

In the rotating RTI, an important dimensionless parameter is the Rossby number. Its expression is as follows [16]:

$$\text{Ro} = U / (2\Omega L_z), \quad (3)$$

where the Rossby number Ro denotes the relative strength of the inertial forces to the Coriolis force. The characteristic velocity U equals to $\sqrt{g\beta\Theta L_z}$ and L_z is the height of the computational domain. In the initial time, the effect of rotation can be negligible, thus $\text{Ro} = 1/(\Omega t)$ is obtained.

B. Lattice Boltzmann method

To solve Eqs. (1) and (2) the double distribution approach (DDF) [22] of LBM is implemented in this paper. Instead of solving the governing equations directly, it solves two coupled distribution functions: the density distribution function (f_i) and internal energy distribution function (g_i). These two distribution functions will be introduced in the following subsection. The mesoscopic evolution equation for the flow field is [23,24]

$$f_i(\mathbf{x} + \mathbf{c}_i \Delta t, t + \Delta t) - f_i(\mathbf{x}, t) = -\omega_f [f_i(\mathbf{x}, t) - f_i^{(\text{eq})}(\mathbf{x}, t)] + F_i \Delta t, \quad (4)$$

where f_i is the density distribution function, $f_i^{(\text{eq})}$ is the equilibrium function, \mathbf{c}_i is the i the discretized velocity vector, ω_f is relaxation parameter [25,26], and F_i is the discrete force term. The evolution equation illustrates a relaxation process. The density distribution function f_i relaxes towards the equilibrium distribution function $f_i^{(\text{eq})}$. The equilibrium function for flow field has the second-order Maxwell distribution form, which can be expressed as

$$f_i^{(\text{eq})}(\mathbf{x}, t) = w_i \rho \left[1 + \frac{\mathbf{c}_i \cdot \mathbf{u}}{c_s^2} + \frac{\mathbf{u}\mathbf{u}}{2c_s^2} : \left(\frac{\mathbf{c}_i \mathbf{c}_i}{c_s^2} - \mathbf{I} \right) \right], \quad (5)$$

where c_s is the sound speed and w_i is the weight coefficient. The D3Q19 model is defined as

The force model proposed by He *et al.* [27] is adopted by the following formula:

$$F_i = \left(1 - \frac{\omega_f}{2} \right) \frac{(\mathbf{c}_i - \mathbf{u}) \cdot \mathbf{G}}{\rho c_s^2} f_i^{(\text{eq})}, \quad (9)$$

where G is the external force. With the consideration of force model [28,29], the velocity $\mathbf{u} = \sum_i f_i \mathbf{c}_i + \frac{\mathbf{G}\Delta t}{2\rho}$. In this paper the external force is consist with both buoyancy and Coriolis force.

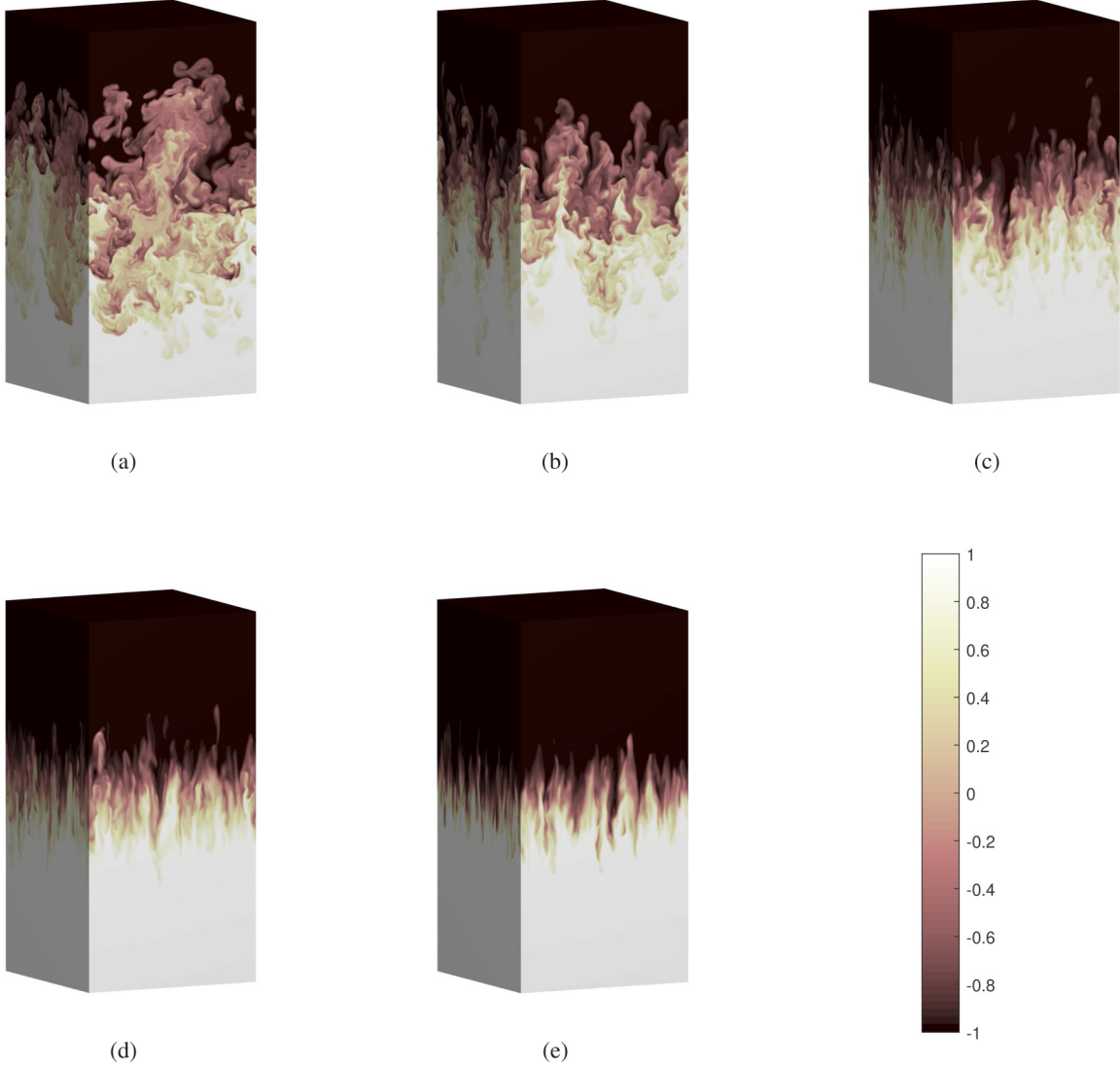


FIG. 1. Snapshots of the temperature field for five simulations with (a) $\Omega\tau = 0$, (b) $\Omega\tau = 5$, (c) $\Omega\tau = 10$, (d) $\Omega\tau = 15$, and (e) $\Omega\tau = 20$ at time $t/\tau = 4$. White (black) denotes the hot (cold) fluid.

The mesoscopic evolution equation of the temperature field is

$$g_i(\mathbf{x} + \mathbf{c}_i \Delta t, t + \Delta t) - g_i(\mathbf{x}, t) = -\omega_g [g_i(\mathbf{x}, t) - g_i^{(\text{eq})}(\mathbf{x}, t)], \quad (10)$$

where the equilibrium distribution function $g_i^{(\text{eq})}$ for the temperature field is given as [25]

$$g_i^{(\text{eq})} = w_i \rho \theta \left[1 + \frac{\mathbf{c}_i \cdot \mathbf{u}}{c_s^2} + \frac{\mathbf{u}\mathbf{u}}{2c_s^2} : \left(\frac{\mathbf{c}_i \mathbf{c}_i}{c_s^2} - \mathbf{I} \right) \right]. \quad (11)$$

The macroscopic temperature (θ) can be calculated by

$$\theta = \frac{1}{\rho} \sum_i g_i. \quad (12)$$

The relation between the relaxation parameter ω_g and thermal diffusivity κ is

$$\kappa = c_s^2 \left(\frac{1}{\omega_g} - \frac{1}{2} \right) \Delta t. \quad (13)$$

Using the Chapman-Enskog technique, one may obtain the traditional governing equations Eqs. (1) and (2) from Eqs. (4) and (10), under the approximation of incompressible flow.

The thermal lattice Boltzmann method is used to simulate the rotating RTI and numerically investigate the small-scale characteristics and scaling law of the rotation effect on the 3D turbulent RTI. To quantitatively discuss the mixing process, results are made dimensionless by the height of computational domain L_z and the dimensionless time $\tau = \sqrt{2L_z/(g\beta\Theta)}$. The rotation is quantified by the dimensionless rotation $\Omega\tau$. Simulations at $\text{Ra} = 10^9$ and $\text{Pr} = 1$, when the $\Omega\tau = 0, 5, 10, 15$, and 20 are implemented. The initial temperature field is defined in Eq. (14)

$$\theta(x, y, z, t = 0) = -\text{sgn}(z - L_z/2)\Theta/2, \quad (14)$$

where $\text{sgn}(x)$ is the sign function. It gives the Atwood number [30] $A = \beta\Theta/2$. In all simulated cases AgL_z is kept at 0.0033 and the resolution is set to $256 \times 256 \times 512 (L_x \times L_y \times L_z)$. The dimensionless initial temperature of the bottom half is equal to 1 and the dimensionless initial temperature of top

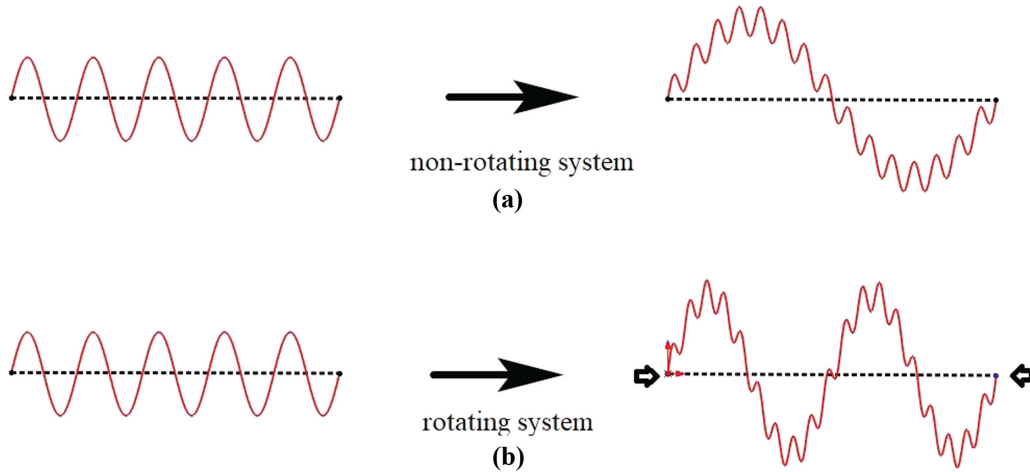


FIG. 2. Schematic of the perturbation evolution in Rayleigh-Taylor system. Panel (a) is a nonrotating system. Panel (b) is a rotating system

half is equal to -1 . The boundary conditions of all cases are as follows. The bottom and top boundaries are isothermal nonslip walls. The implementation of this boundary condition in DDF can be expressed as

$$f_i(\mathbf{x}, t + \Delta t) = f_i^+(\mathbf{x}, t), \quad (15)$$

$$g_i(\mathbf{x}, t + \Delta t) = 2w_i\rho\theta_w - g_i^+(\mathbf{x}, t), \quad (16)$$

where \mathbf{c}_i represents the inverse direction of velocity \mathbf{c}_i , i.e., $\mathbf{c}_i = -\mathbf{c}_i$. The subscript $+$ represents the density distribution function after the collision step and before the streaming step. θ_w is the specific temperature at the isothermal wall. The left, right, front, and back boundaries are periodic boundaries. Taking the density distribution function f_i as an example, it can be expressed as

$$f_i(\mathbf{x}, t + \Delta t) = f_i^+(\mathbf{x} - \mathbf{c}_i\Delta t + L_x\mathbf{n}_x, t + \Delta t), \quad (17)$$

where \mathbf{n}_x is the unit vector along the x axis.

III. RESULTS AND DISCUSSIONS

The temperature, the mixing zone width $h(t)$, the root mean square (RMS) of velocity and temperature, the heat transfer efficiency, energy spectra, and structure function will be discussed with increasing $\Omega\tau$ in the rest of this section.

A. Snapshot of temperature

Figure 1 describes the snapshots of the temperature field for four simulations obtained at time $t/\tau = 4$ and at $\Omega\tau = 0$, $\Omega\tau = 5$, $\Omega\tau = 10$, $\Omega\tau = 15$, and $\Omega\tau = 20$. As shown in Fig. 1, the rotation produces clear qualitative effects on the temperature field. The thermal plumes with the plume size decrease geometrically and the mixing layer increasingly decreases with increasing $\Omega\tau$. It is more coherent and elongated for thermal plumes in the vertical direction while their vertical velocity is suppressed. Meanwhile, the thickness of the mixing layer decreases with the increase of $\Omega\tau$ at the same evolution time, which reveals that the effect of rotation is to reduce the growth of the mixing layer, a feature which is consistent with previous studies [16,20]. Boffetta *et al.* [16] argued that when the thickness of the rotating system ($\Omega\tau =$

20) is equal to that of the nonrotating RT turbulence, the rotating system takes much longer than that of the nonrotating RT turbulence.

At first the stability of the interface is broken by high wave-number perturbations (see Fig. 2). As a result, in the early stage, a large number of small-scale plumes form at the interface. With the mixing process of the RTI developing, small plumes are stretched, warped, and merged with each other and form large plumes. The wave length of the large plume is the scale of the energy injection. In the rotating system, under the action of Coriolis force, the horizontal stream bends, thus the horizontal growth of plumes is limited. As a result, the wave numbers of large plumes are smaller than that of the nonrotating system. As the horizontal growth of plumes is limited in the rotating system, the plumes can only be stretched in the vertical direction, and then the aspect ratios of plumes increase with the increase of $\Omega\tau$. With the convection of the rotating system further developing, the vertical growth of plumes is suppressed due to high aspect ratio.

To quantitatively analyze the rotation effect on the growth of the mixing zone, we use the mixing zone width $h(t)$ based on the mean temperature $\langle\theta\rangle_{x,y}$ [31,32],

$$h(t) = \frac{6}{\Theta} \int_0^{L_z} \left(\langle\theta\rangle_{x,y} + \frac{\Theta}{2} \right) \left(\frac{\Theta}{2} - \langle\theta\rangle_{x,y} \right) dz, \quad (18)$$

in which $\langle\cdot\rangle_{x,y}$ denotes the average number on the xOy plane. In this paper, four independent realizations of 3D RT evolution were performed to assess the repeatability of the statistical quantities by adding different perturbed interfaces. The mixing layer width $h(t)$ increases with time evolution. The relation between the $h(t)$ are time t can be obtained by using the assumption in the nonrotating system [33,34]. Its expression is as follows:

$$\sqrt{h(t)} = \sqrt{h_0} + t\sqrt{\alpha Ag}, \quad (19)$$

in which α denotes a dimensionless value [6,7], A is the Atwood number ($A = \beta\Theta/2$), and h_0 denotes the width of the initial temperature jumping zone. To obtain the effect of rotation on the global quantities in the turbulent RT mixing zone, the mixing zone width $h(t)$ is studied at various

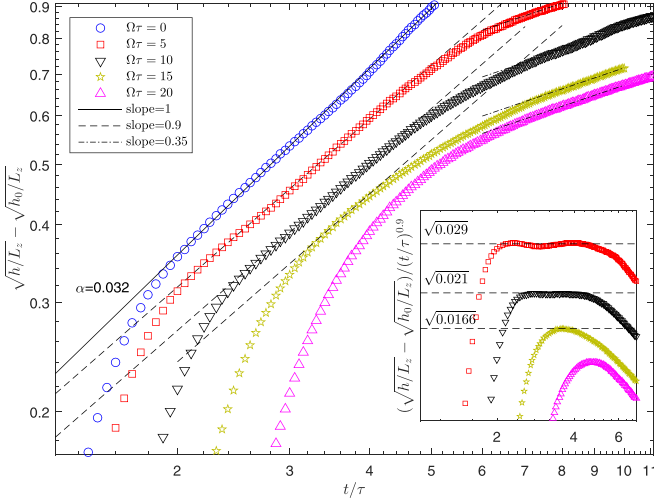


FIG. 3. Temporal growth of the mixing zone width $h(t)$ at $\Omega\tau = 0$, $\Omega\tau = 5$, $\Omega\tau = 10$, and $\Omega\tau = 20$.

$\Omega\tau$. Figure 3 displays the temporal growth of the mixing zone width $h(t)$ at $\Omega\tau = 0$, $\Omega\tau = 5$, $\Omega\tau = 10$, $\Omega\tau = 15$, and $\Omega\tau = 20$. It is demonstrated that a linear slope 1 of the mixing zone width $\sqrt{h(t)/L_z} - \sqrt{h_0(t)/L_z}$ and the parameter $\alpha = 0.032$ under the nonrotation condition is obtained in a range with time evolution ($1.8 < t/\tau < 5.6$), which is consistent with previous work [6,7,30,35]. The $t^{0.9}$ scaling law for the mixing zone width $\sqrt{h(t)/L_z} - \sqrt{h_0(t)/L_z}$ at $\Omega\tau = 5$ and $\Omega\tau = 10$. The $t^{0.35}$ scaling law for the mixing layer width $\sqrt{h(t)/L_z} - \sqrt{h_0(t)/L_z}$ at $\Omega\tau = 20$ is obtained. The mixing zone width $h(t)$ decreases with the increase of $\Omega\tau$ at the same time, which reveals that the rotation suppresses the mixing layer width $h(t)$. In the inset of Fig. 3, we can see that the time region of satisfying a slope 0.9 of the mixing zone width for $\Omega\tau = 10$ ($2.5 < t/\tau < 4.5$) is less than that of $\Omega\tau = 5$ ($2 < t/\tau < 5$), which reveals that the time in the region meeting this scaling law is gradually narrowing. The above phenomenon further indicates that the isotropic convective mixing dominates at $\Omega\tau = 0$. However, in the rotating system, the mixing layer is transverse isotropic. The behavior of $h(t)$ follows the $t^{0.9}$ scaling law in the early time, which can be seen in Fig. 3. The 0.9 scaling law can be obtained as

$$\sqrt{h(t)} = \sqrt{h_0} + t^{0.9} \sqrt{\alpha Ag}. \quad (20)$$

The 0.9 scaling law range becomes narrow with the increment of $\Omega\tau$. When $\Omega\tau$ is higher than 15, the 0.9 scaling law range disappears. The parameter α is 0.029, 0.021 and 0.0166 for $\Omega\tau = 5$, 10, and 15, respectively. The 0.9 scaling law can hardly be found when $\Omega\tau = 20$.

Figure 4 indicates the $t^{0.35}$ scaling law for the mixing layer width $h(t)$ when t/τ is higher than 7. The new scaling law is

$$\sqrt{h(t)} = \sqrt{h_0} + t^{0.35} \sqrt{\alpha Ag}. \quad (21)$$

The parameter α equals to 0.193, 0.137, 0.102, and 0.09 for $\Omega\tau = 5$, 10, 15, and 20, respectively. As analyzed before, the Coriolis force in a rotating system suppresses the horizontal development of fluctuations and breaks the spikes into small wavelength ones. However, the vertical development of fluctuation is accelerated by the rotating effect. The develop-

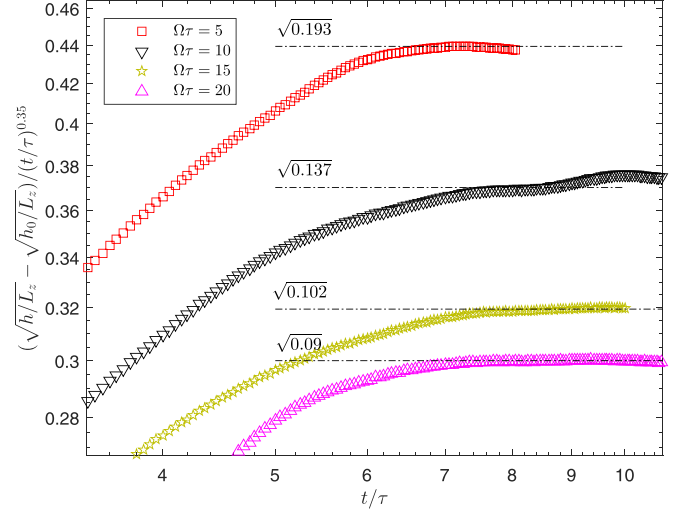


FIG. 4. Temporal growth of the mixing zone width $h(t)$ at $\Omega\tau = 5$, $\Omega\tau = 10$, $\Omega\tau = 15$, and $\Omega\tau = 20$.

ment process of small-scale motion will be analyzed in the following section in detail. As a result, the fluctuations reach the bottom and top boundaries and bounce back from the boundaries earlier in the rotating system. The second scaling law is formed under all the effects of the buoyancy, the Coriolis force, and the reflected fluctuation.

Figure 5 shows the mean temperature profiles of the horizontal surfaces obtained at time $t/\tau = 4$ and at $\Omega\tau = 0$, $\Omega\tau = 5$, $\Omega\tau = 10$, $\Omega\tau = 15$, and $\Omega\tau = 20$. As shown in Fig. 5, the mean temperature profile $\langle\theta\rangle_{x,y}$ is approximately linear within the mixing layer at $t/\tau = 4$. With the increase of $\Omega\tau$, the slope of the temperature profile increases, which reveals that the convection is suppressed by rotation. In the same sample size, by comparing the velocity profiles with rotation and without rotation, it can be seen that the more intense the rotation, the smoother the statistical results of the velocity profile. It reveals that the maximum characteristic scale of convection decreases

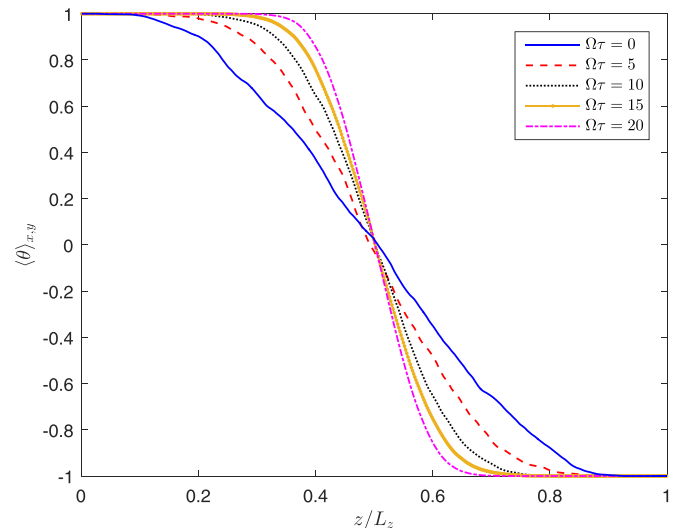


FIG. 5. Mean temperature profiles $\langle\theta\rangle_{x,y}$ at $t/\tau = 4$ in cases of different $\Omega\tau$.

with the increase of $\Omega\tau$. The effect of rotation on the velocity and temperature of mixing zone will be further studied in the following subsection.

B. Effect of rotating on global quantities in mixing zone

The efficiency of heat transfer in the RT turbulence mixing zone is evaluated by the Nusselt number [6,11,12]

$$\text{Nu} = 1 + \langle w\theta \rangle L_z / (\Theta\kappa). \quad (22)$$

The functional relation between Nu and Ra has been widely studied by direct numerical simulations in the RT turbulence [2,4,36].

$$\text{Nu} \simeq \text{Ra}^{1/2} \text{Pr}^{1/2}. \quad (23)$$

The Reynolds number is defined as $\text{Re} = \sqrt{u_{\text{rms}}^2 + v_{\text{rms}}^2 + w_{\text{rms}}^2} h / \nu$. The relation between Re and Ra has also been displayed by both two and three direct numerical simulations in the RT turbulence [1,2,4,7]

$$\text{Re} \simeq \text{Ra}^{1/2} \text{Pr}^{-1/2}. \quad (24)$$

In the RT turbulent mixing zone, the turbulent convection is dominated by the bulk dynamics and the ultimate state observation is not amazing as upper and lower boundaries play no role in the mixing zone system [37]. The effect of rotation on the relations of Nu-Ra and Re-Ra is studied in this paper. Figure 6 displays the Nusselt number and Reynolds number as functions of the Rayleigh number for $\Omega\tau = 0$ (black circle and line), $\Omega\tau = 5$ (blue circle and line), $\Omega\tau = 10$ (red circle and line), and $\Omega\tau = 20$ (purple circle and line). The black solid line represents the theoretical value. As displayed in Fig. 6, for $\Omega\tau = 0$, the 1/2 scaling law for Nu-Ra and Re-Ra is obtained in the RT turbulent mixing zone, which is consistent with the theory proposed by Grossmann and Lohse [38], and the previous numerical simulations [1,4,7,8]. The value of Nu as a function of Ra decreases with increasing $\Omega\tau$, which reveals that the heat transfer efficiency is reduced by the rotation. We also see that Re also decreases with the increase of $\Omega\tau$ at the same Ra. It is apparent that the relations of both Nu and Ra as a function of Ra are not increasingly satisfied with the linear scaling of the ultimate state ($\text{Ra}^{1/2}$), which is obviously lower than $\text{Ra}^{1/2}$ with increasing $\Omega\tau$. As Ra increases, the decline gradient of the relations of both Nu and Ra increases, which reveals that the heat transfer performance is increasingly suppressed with increasing Ra by the rotation in the RT mixing zone. The above phenomenon is also demonstrated by previous direct numerical simulations [16]. The heat transport suppression by the rotation is qualitatively different from that of rotating Rayleigh-Bénard (RB) convection by the rotating boundary force [6,16,36].

The mixedness of the RT system can be measured by the mixed mass. Based on the definition of mixed mass [14] and the Boussinesq approximation, the expression can be rewritten as

$$\Psi = \frac{\int_V (\theta + \frac{\Theta}{2}) (\frac{\Theta}{2} - \theta) dv}{\int_V ((\theta)_{x,y} + \frac{\Theta}{2}) (\frac{\Theta}{2} - (\theta)_{x,y}) dv}, \quad (25)$$

where subscript V represents the entire computational domain. Figure 7(a) shows the temporal evolution of Ψ in the

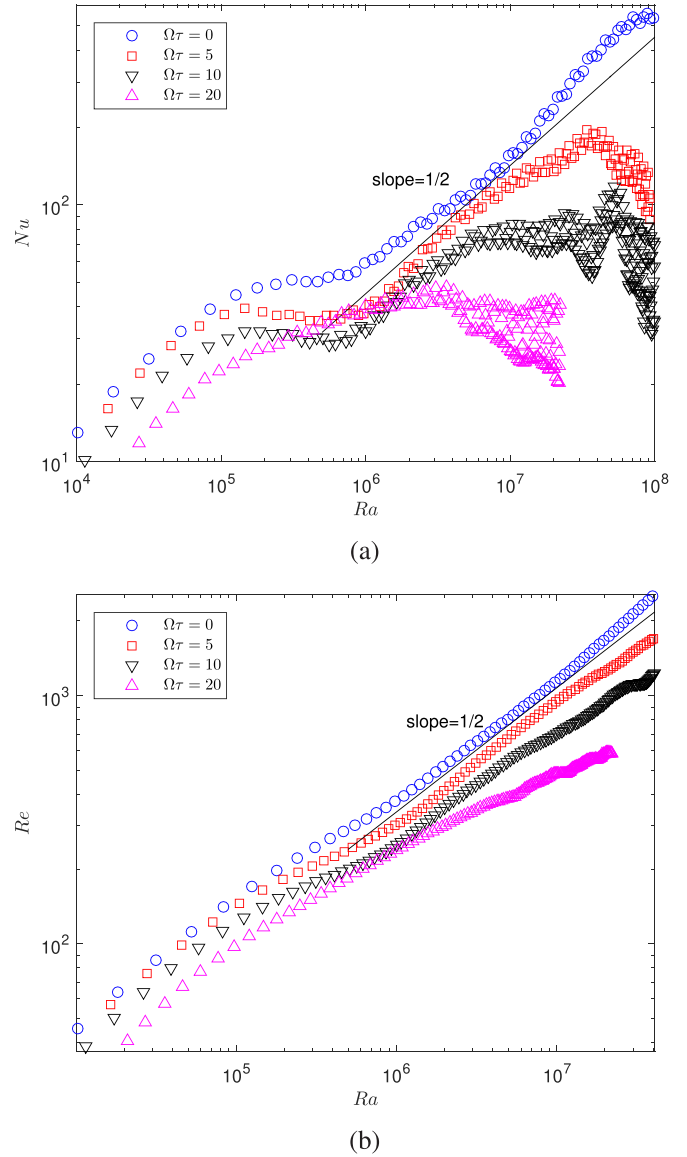


FIG. 6. (a) Nusselt number and (b) Reynolds number are shown as functions of Rayleigh number for $\Omega\tau = 0$ (black circle and line), $\Omega\tau = 5$ (blue circle and line), $\Omega\tau = 10$ (red circle and line), and $\Omega\tau = 20$ (purple circle and line). The black solid line represents the theoretical value.

cases of different $\Omega\tau$. At first, the mixed mass Ψ for the nonrotating system decreases rapidly and reaches the minimum point of about 0.55 at $t/\tau = 1.5$. After that, Ψ increases to about 0.8 and then becomes stable. This agrees well with previous studies [14]. In the rotating system, the evolution of Ψ is essentially the same as that in a nonrotating system, except all periods are delayed. The relation of mixed mass versus the height of the mixing layer is also shown in Fig. 7(b). Except for $\Omega\tau = 5$, Ψ in other systems reaches the minimum value at about $h/L_z = 0.1$. We also believe that, with enough resolution, the mixing mass Ψ in the case of $\Omega\tau = 5$ will reach the minimum value at about $h/L_z = 0.1$. It illustrates the existence of an initial acceleration mixing period. The period exceeds the equilibrium state and then returns back to

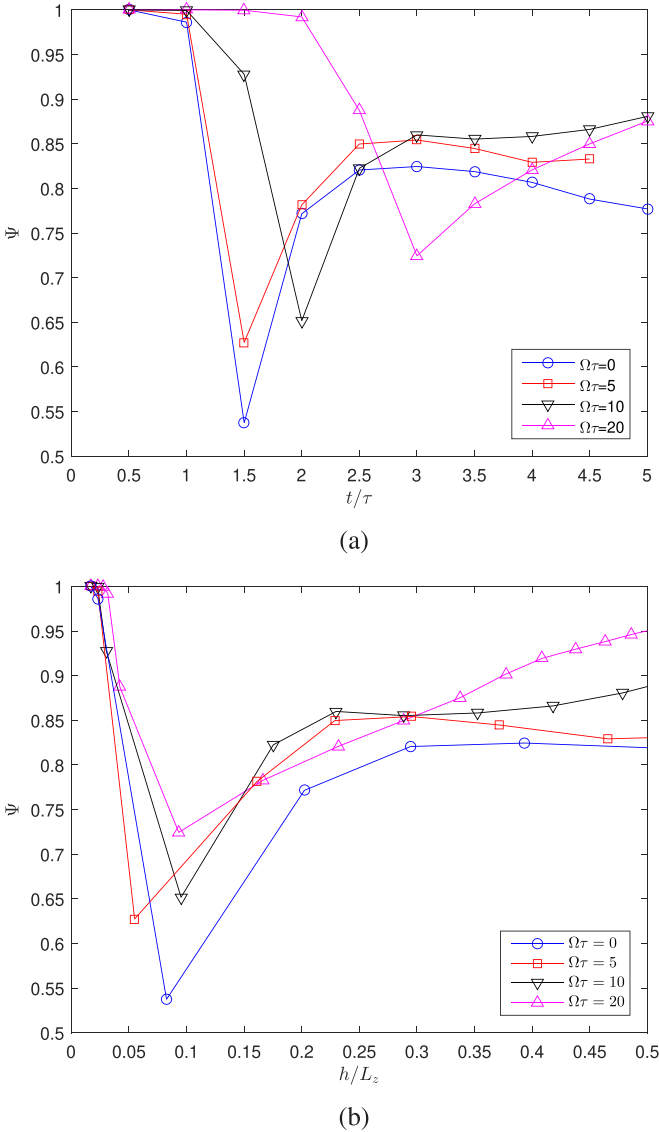


FIG. 7. Temporal evolution of mixed mass for different $\Omega\tau$. Mixed mass are shown as functions of (a) dimensionless time t/τ and (b) dimensionless height of mixing layer h/L_z .

the equilibrium state. Figure 7(b) proves that the initial period is related to the height of the mixing layer.

The temporal evolution of the skewness for different $\Omega\tau$, which is shown in Fig. 8, also proves the existence of the initial acceleration process. The definition of skewness is [16]

$$S_w = \frac{\langle \omega_z^3 \rangle}{\langle \omega_z^2 \rangle^{3/2}}. \quad (26)$$

The dimensionless time of the initial period shown by the skewness in Fig. 8 is consistent with that shown by the mixed mass in Fig. 7. In the initial period, the mixed mass and skewness first developed gently. After a while, the skewness jumps to the maximum value under the Coriolis force. Meanwhile, the mixed mass continually gets smaller. With the mixing process further developed, the mixed mass reaches its minimum value and the skewness keeps rapidly getting smaller. At the end of the initial period, both the mixed mass and

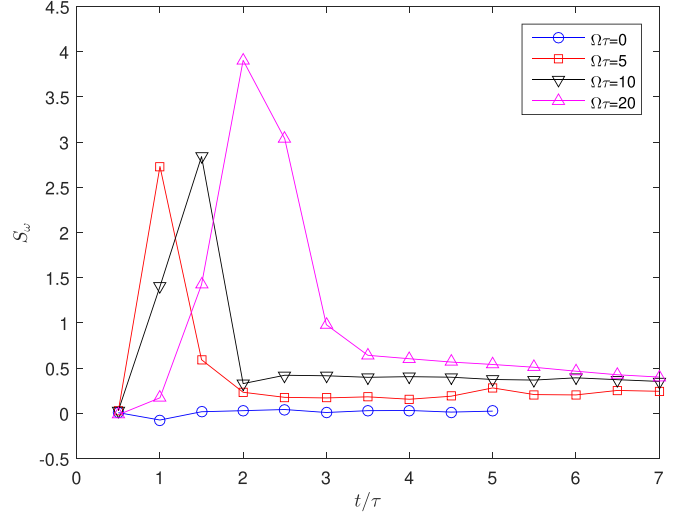


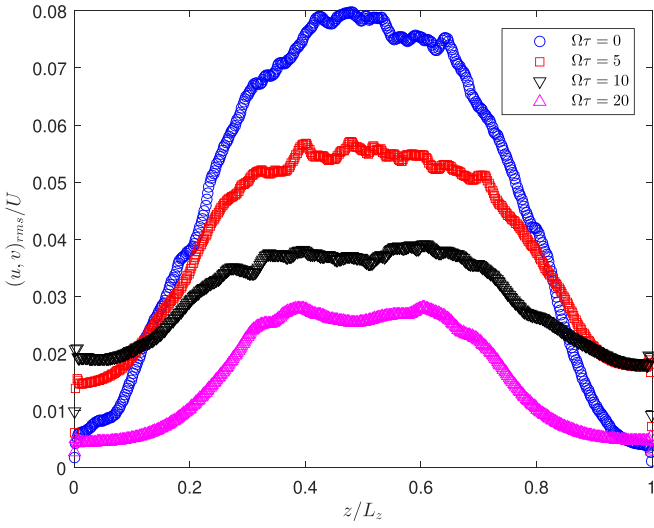
FIG. 8. Temporal evolution of the skewness for different $\Omega\tau$.

the skewness approach a stable number. The stable skewness increases with the increase of $\Omega\tau$.

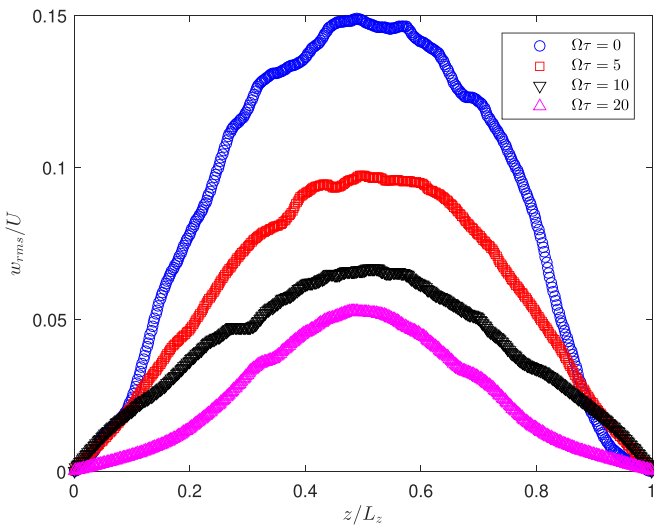
C. Root mean square of velocity and temperature fluctuation

To better understand the behavior of the temporal evolution of the rotating RT system, the comparison of the RMS of the velocity fluctuation between the rotating and nonrotating systems are shown in Fig. 9.

Figure 9 describes the mean vertical profiles of the RMS of horizontal velocity $(u, v)_{\text{rms}}$ and the RMS of vertical velocity w_{rms} obtained at time $t/\tau = 4$ in the cases of $\Omega\tau = 0$, $\Omega\tau = 5$, $\Omega\tau = 10$, and $\Omega\tau = 20$, where $i_{\text{rms}} = \sqrt{\langle (i - \langle i \rangle_V)^2 \rangle}$ is the RMS of i with $i = u, v, w$ or θ . As described in Fig. 9, it is seen that the amplitudes of the $(u, v)_{\text{rms}}$ and w_{rms} obviously decrease with the increase of $\Omega\tau$ in the mixing zone. Moreover, the gradients of these quantities sharply decrease with increasing $\Omega\tau$ in the mixing zone, which further demonstrates that the growth of the mixing layer is reduced by the rotation. In Fig. 9(a) The effect of rotation on the propagation of the horizontal perturbation is further illustrated by comparing the RMS of the horizontal velocity fluctuation between the rotating system and nonrotating system. The horizontal propagation of the horizontal fluctuation is suppressed by the Coriolis force. With the increment of $\Omega\tau$, the RMS of horizontal fluctuation decreases in the mixing zone. The vertical propagation of the horizontal fluctuation is motivated by both vertical perturbation and horizontal shear force. From Fig. 9(b), it is seen that the vertical perturbation is also suppressed by the rotation effect. The RMS of the horizontal fluctuation near the bottom and top boundaries in Fig. 9(a) shows the rotating effect on the vertical propagation of horizontal perturbation. When $\Omega\tau$ is less than 10, the shear force is strengthened by the rotation effect. Compared with the shear force strength, the intensity of the vertical fluctuation suppression is smaller. The propagation process is accelerated by the rotating effect. When $\Omega\tau$ further increases, the influence of the vertical fluctuation suppression increases. The vertical propagation process is suppressed.



(a)



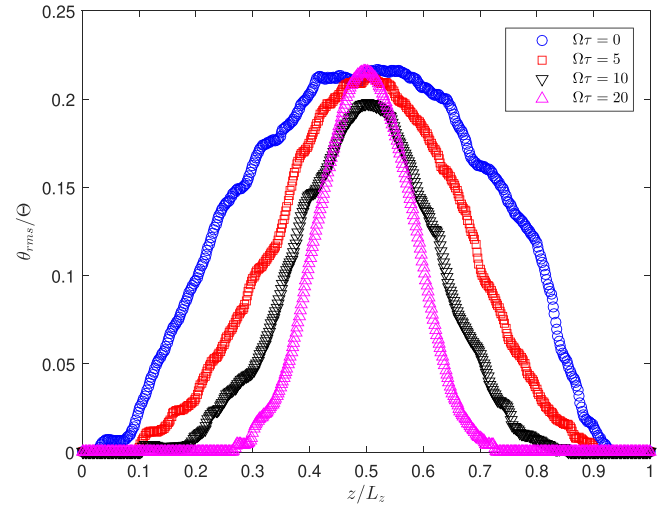
(b)

FIG. 9. The comparison of the RMS between (a) horizontal velocity $(u, v)_{\text{rms}}$ and (b) vertical velocity w_{rms} at $t/\tau = 4$ in cases of different $\Omega\tau$.

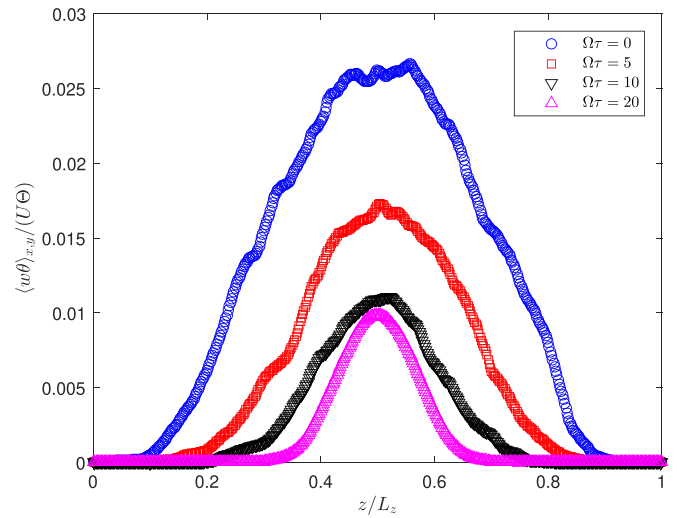
Figure 10 displays the mean vertical profiles of the RMS of temperature θ_{rms} and the heat flux $\langle w\theta \rangle_{x,y}$ obtained at time $t/\tau = 4$ in the cases of $\Omega\tau = 0$, $\Omega\tau = 5$, $\Omega\tau = 10$, and $\Omega\tau = 20$. As displayed in Fig. 10, it is clearly observed that the amplitudes of the RMS of temperature θ_{rms} and the amplitudes of the heat flux $\langle w\theta \rangle_{x,y}$ obviously decrease with the increase of $\Omega\tau$ in the mixing zone. Moreover, the gradients of these quantities sharply decrease with increasing $\Omega\tau$ in the mixing zone, which further demonstrates that the temperature growth of the mixing layer is reduced by the rotation.

D. Probability density function of velocity and temperature fluctuations

The Kolmogorov-Obukhov theory of Navier-Stokes turbulence can be obtained based on an assumption in three



(a)



(b)

FIG. 10. Mean vertical profiles of the RMS of (a) temperature fluctuation θ_{rms} , (b) the heat flux fluctuation $\langle w\theta \rangle_{x,y}$ at $t/\tau = 4$ in cases of different $\Omega\tau$.

dimensions. The velocity fluctuation δu_r is named the inertial interval in a range of scales $\eta \ll r \ll L(t)$. Figure 11 illustrates the probability density functions of the horizontal and vertical velocity fluctuations at different $\Omega\tau = 0$, $\Omega\tau = 5$, $\Omega\tau = 10$, and $\Omega\tau = 20$ at time $t/\tau = 4$. As illustrated in Fig. 11, the horizontal velocity fluctuation gradually decreases with the increase of $\Omega\tau$, and the vertical velocity fluctuation also decreases with increasing $\Omega\tau$, which reveals that the rotation effectively suppresses the turbulent velocity fluctuations. Meanwhile, the distribution function of the probability density function (PDF) for the vertical velocity fluctuation is increasingly concentrated in the central core. The decrease of the above velocity fluctuation can be caused by increasing Coriolis force $2\boldsymbol{\omega} \times \mathbf{u}$. The Coriolis force accelerates the large-scale vortex breaking to the small-scale vortex.

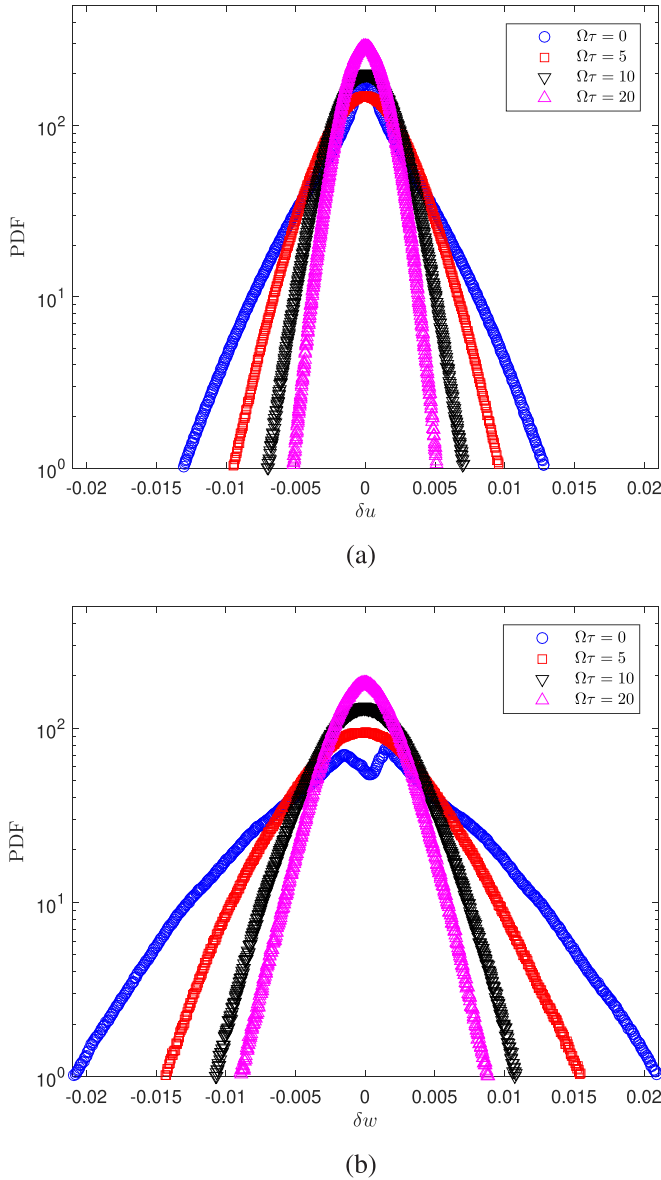


FIG. 11. Probability density functions of (a) horizontal velocities fluctuation and (b) vertical velocities fluctuation in cases of different $\Omega\tau$ at time $t/\tau = 4$.

Figure 12 displays the PDF of the temperature fluctuation at different $\Omega\tau$ when dimensionless time $t/\tau = 4$. It is seen that the distribution function of PDF for the fluctuation of temperature increasingly concentrates in the central core. The fluctuation of temperature decreases with the increase of $\Omega\tau$, which reveals that the fluctuation of temperature is suppressed by the rotation. In the following section, the energy spectrum of velocity and temperature fluctuations is further studied at different $\Omega\tau$.

E. Kinetic and temperature energy spectra

Chertkov [9] proposed a theory of turbulent fluctuations for RT turbulence, predicted a Kolmogorov-Bukhov (K41) scenario for velocity and temperature spectra in 3D space, and a Bolgiano-Obukhov-like (BO59) scenario in two-dimensional

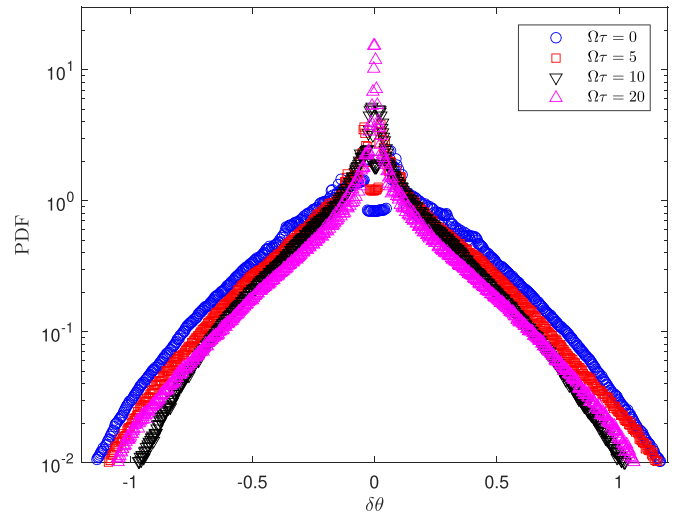


FIG. 12. Probability density functions of temperature fluctuation at $\Omega\tau = 0$, $\Omega\tau = 5$, $\Omega\tau = 10$, $\Omega\tau = 15$, and $\Omega\tau = 20$.

(2D) space [7]. The dimensional predictions of the spatial and temporal domains can be obtained for both velocity and temperature fluctuations by the relationships of scaling in Eqs. (27) and (28) for the 3D case [6]. These predictions can be obtained to build the scaling laws of isotropic spectra by neglecting possible fluctuations of intermittency. The kinetic and temperature energy spectra are obtained in the 3D case [6]

$$E_u(k) \sim (\beta g \theta_0)^{4/3} t^{2/3} k^{-5/3}, \quad (27)$$

$$E_\theta(k) \sim \theta_0^2 (\beta g \theta_0)^{-2/3} t^{-4/3} k^{-5/3}. \quad (28)$$

Figure 13 shows the kinetic energy spectra E_{uv} and E_w obtained in the mixing zone at time $t/\tau = 4$ under $\Omega\tau = 0$, $\Omega\tau = 5$, $\Omega\tau = 10$, and $\Omega\tau = 20$. As displayed in Fig. 13, the values of the kinetic energy spectra E_{uv} and E_w obviously decrease with the increase of $\Omega\tau$ in the mixing zone. The wave number of the energy injection peak gradually increases with the increase of $\Omega\tau$, which reveals that the energy injection scale decreases with the increase of $\Omega\tau$. The energy injection scale is related to the wave length of the large plumes. The decrease of the energy injection scale further proves the physical mechanism of the rotation effect suppressing the horizontal development of plumes, which is shown in Fig. 2.

Figure 14 illustrates the temperature energy spectra $E_\theta(k)$ obtained on the middle horizontal plane when $h/L_z \approx 0.7$ in the cases of $\Omega\tau = 0$, $\Omega\tau = 5$, $\Omega\tau = 10$, and $\Omega\tau = 20$. As illustrated in Fig. 14, it is clearly observed that the values of the temperature energy spectra $E_\theta(k)$ obviously decrease with increasing $\Omega\tau$ in the mixing zone. The scale of the energy injection decreases due to the rotation effect. Meanwhile, the dissipation scale, i.e., the Kolmogorov scale η increases with the increase of $\Omega\tau$. From the following relation, one may conclude that the turbulence dissipation rate ε decreases with the increase of $\Omega\tau$:

$$\eta \sim \left(\frac{v^3}{\varepsilon} \right)^{1/4}. \quad (29)$$

Thus, the width of the inertial subrange with power of $-5/3$ for $E_u(k)$ dramatically narrows at $t/\tau = 4$. The thermal

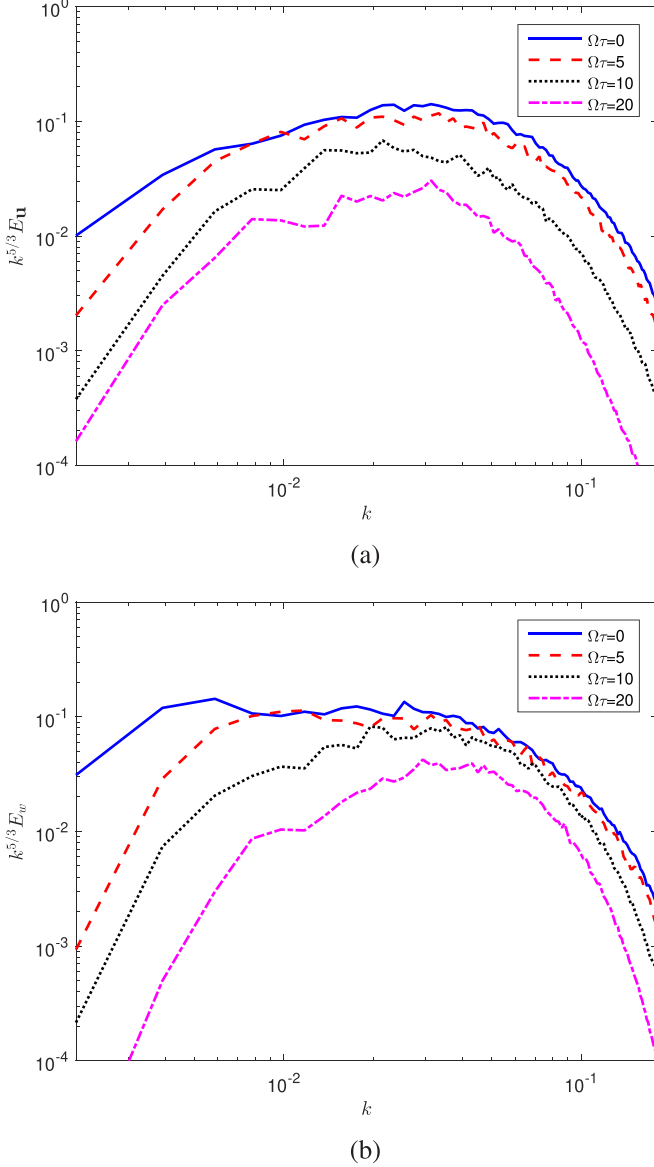


FIG. 13. Compensated kinetic energy spectra of (a) horizontal velocity $E_u(k)$ and of (b) vertical velocity $E_w(k)$ for $\Omega\tau = 0$, $\Omega\tau = 5$, $\Omega\tau = 10$, and $\Omega\tau = 20$.

spectra $E_\theta(k)$ shows the same characteristics as the kinetic spectra, which further demonstrates that the turbulence intensity is suppressed by the rotation.

F. Spatial scaling law of structure function

In the nonrotation RT turbulence, Zhou *et al.* [1] provided a deep analysis on the distribution of the local dissipation scale in 2D RT turbulence. Zhou *et al.* [7] studied the second, fourth, and sixth order structure functions of the velocity and temperature, and the curves for the second structure functions were closely consistent with the Chertkov [9] theory for both the spatial and temporal scaling in 2D space. Biferale *et al.* [4] and Zhou [7] confirmed these corrections of intermittency by direct numerical simulation (DNS) in 2D space. Nevertheless, the velocity and temperature structure functions for velocity

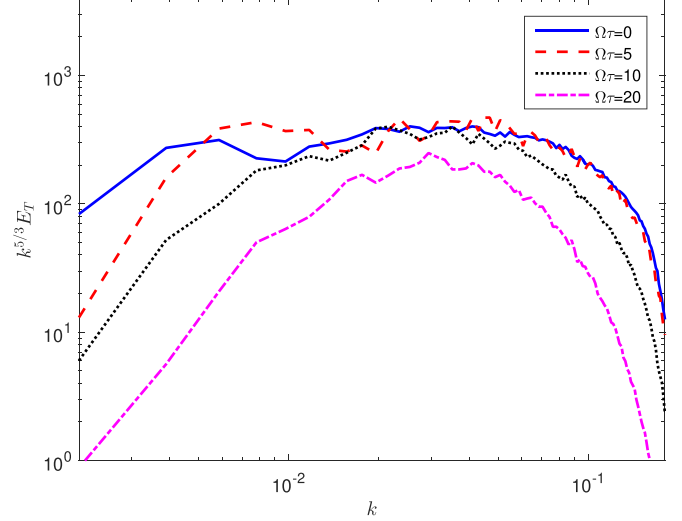


FIG. 14. Compensated temperature energy spectra $E_\theta(k)$ for $\Omega\tau = 0$, $\Omega\tau = 5$, $\Omega\tau = 10$, and $\Omega\tau = 20$.

and temperature fluctuations are given, neglecting the possible intermittency fluctuations in the 3D case [4]

$$S_p^U(r) = \left\langle \left[\left[\mathbf{u}(\mathbf{r}, t) - \mathbf{u}(0, t) \right] \cdot \frac{\mathbf{r}}{r} \right]^p \right\rangle \simeq (\beta \mathbf{g} \theta_0)^{-2p/3} t^{p/3} r^{p/3}, \quad (30)$$

$$S_p^\theta(r) = \langle \{ [\theta(\mathbf{r}, t) - \theta(0, t)] \}^p \rangle \simeq \theta_0^p (\beta \mathbf{g} \theta_0)^{-p/3} t^{-2p/3} r^{p/3}. \quad (31)$$

In this paper, the second, fourth, and sixth order structure functions of the velocity and temperature are investigated in 3D space. Figure 15 displays the structure function of the second order velocity S_2^U and the structure function of temperature S_2^θ obtained in the mixing zones, at time $t/\tau = 4$ and $\Omega\tau = 0$, $\Omega\tau = 5$, $\Omega\tau = 10$, and $\Omega\tau = 20$, where these values are obtained by space averages in the mixing zone under the small-scale isotropy and homogeneity hypothesis. As displayed in Fig. 15, one can see that for nonrotation ($\Omega\tau = 0$), two scaling laws of $2/3$ for the second order velocity and temperature structure functions appear in a range scale, and closely agree with the theory proposed by Chertkov [9] for the spatial scaling in 3D space, respectively. Meanwhile, it is also observed that the values of the velocity and temperature second structure functions gradually decrease with the increase of $\Omega\tau$, which reveals that the spatial intermittency fluctuations of the velocity and temperature are increasingly suppressed by the rotation. Interestingly, it is found that the scale satisfying the linear relationship ($2/3$ scaling law) for second order velocity and temperature structure functions is gradually narrowing with increasing $\Omega\tau$ at time $t/\tau = 4$.

Figures 16 and 17 show the structure function of fourth (S_4^U) and sixth order velocities (S_6^U) and the structure function of fourth (S_4^θ) and sixth order temperatures (S_6^θ) obtained in the mixing zones at time $t/\tau = 4$ and $\Omega\tau = 0$, $\Omega\tau = 5$, $\Omega\tau = 10$, and $\Omega\tau = 20$, respectively. In the nonrotation ($\Omega\tau = 0$) system, two scaling laws of $4/3$ for the fourth order velocity

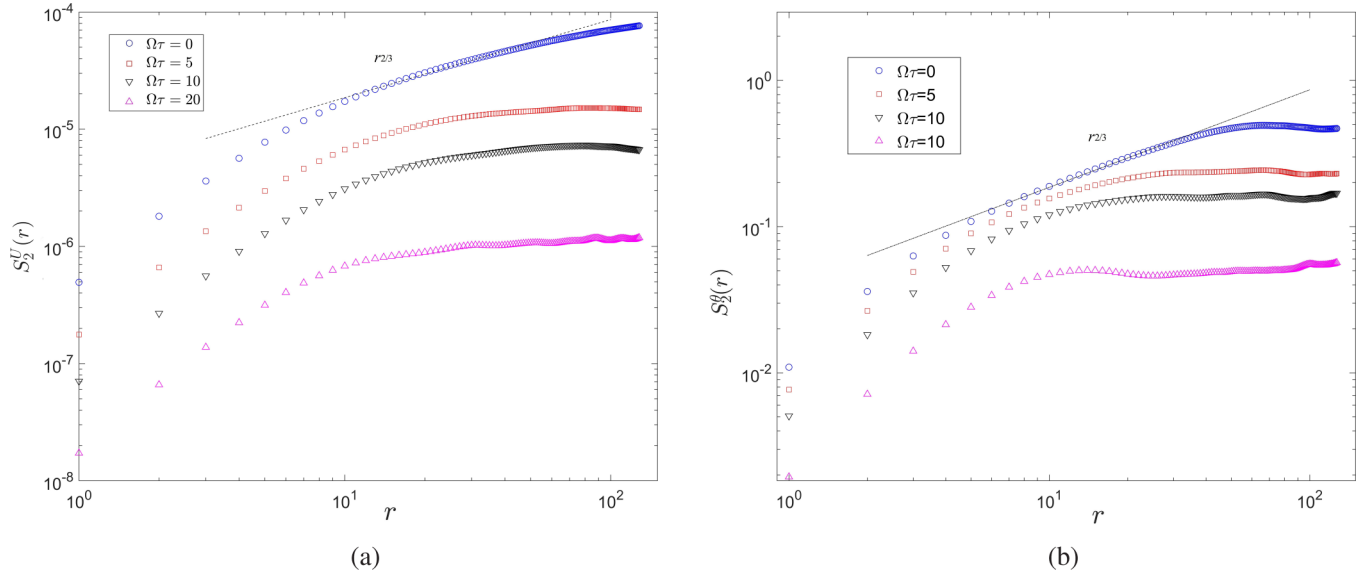


FIG. 15. Second structure function of (a) the velocity $S_2^U(r)$. (b) Second structure function of the temperature $S_2^\theta(r)$ when $\Omega\tau = 0$, $\Omega\tau = 5$, $\Omega\tau = 10$, and $\Omega\tau = 20$.

and temperature structure functions appear in a range scale, a scaling law of power 2 is obtained for the sixth order velocity and temperature structure functions in a range scale, which is consistent with the theory proposed by Chertkov [9] for the spatial scaling in 3D space, respectively. Nevertheless, with the increase of $\Omega\tau$, the fourth and sixth order velocity and temperature structure functions gradually decrease at the same scale. In addition, the width of the linear relationships for the fourth and sixth order velocity and temperature structure functions decreasingly narrow with increasing $\Omega\tau$. This further demonstrates that the spatial intermittency fluctuations of the velocity and temperature are increasingly suppressed by the rotation. These phenomena may be due to inhibiting the speed

mixing of RT turbulence by rotation, which makes the mixing thickness narrow at the same time.

IV. CONCLUSION

In this paper, the evolution of plumes, small-scale fluctuation, and scaling laws of mixing in 3D rotating turbulent RTI are studied. The main conclusions are included as follows.

The size of the thermal plumes and the width mixing layer increasingly decrease with the increase of $\Omega\tau$. The horizontal development of the plumes is suppressed in the rotating system. Thus, the aspect ratio of plumes increase with the increase of $\Omega\tau$.

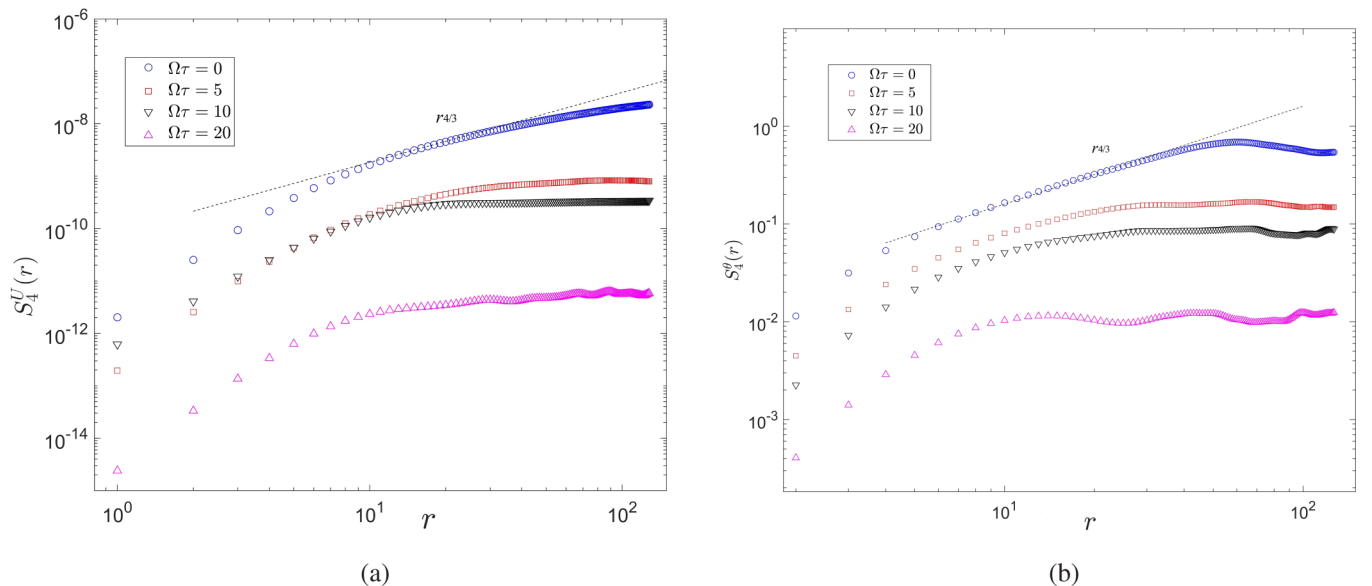


FIG. 16. (a) Fourth structure function of the velocity $S_4^U(r)$. (b) Fourth structure function of the temperature $S_4^\theta(r)$ when $\Omega\tau = 0$, $\Omega\tau = 5$, $\Omega\tau = 10$, and $\Omega\tau = 20$.

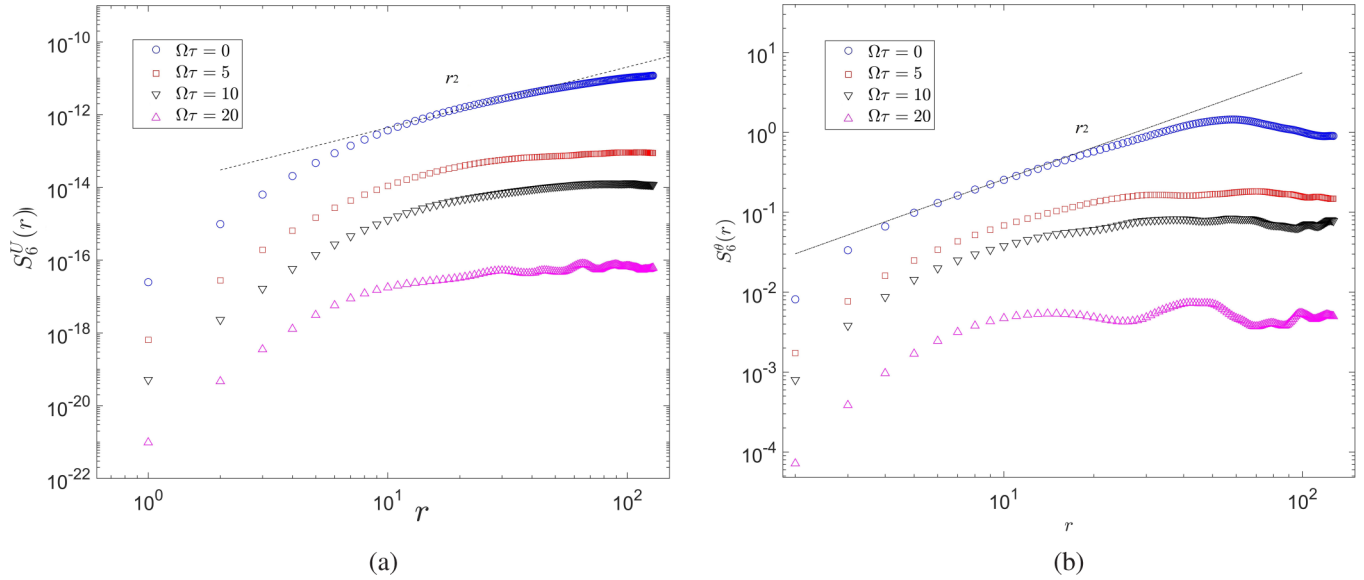


FIG. 17. (a) Sixth structure function of the velocity S_6^U . (b) Sixth structure function of the temperature S_6^θ when $\Omega\tau = 0, \Omega\tau = 5, \Omega\tau = 10,$ and $\Omega\tau = 20$.

The velocity and temperature fluctuations are increasingly reduced with the increase of Coriolis force in the mixing zone. The heat transfer performance is increasingly suppressed with increasing Ra by the rotation in the RT mixing zone. The mixing layer width $h(t)$ gradually decreases with increasing $\Omega\tau$ and the rotation suppresses the mixing layer width $h(t)$. We find two scaling laws in the rotating system. The 0.9 scaling law for the mixing zone width $\sqrt{h(t)/L_z} - \sqrt{h_0(t)/L_z}$ at $\Omega\tau = 5, \Omega\tau = 10,$ and $\Omega\tau = 15,$ and a scaling law of power 0.35 for the mixing zone width $\sqrt{h(t)/L_z} - \sqrt{h_0(t)/L_z}$ at $\Omega\tau = 5, \Omega\tau = 10, \Omega\tau = 15,$ and $\Omega\tau = 20$ are obtained with time evolution.

The energy spectra indicates that the energy injection scale decreases and the Kolomogrov scale η increases with the increase of $\Omega\tau$. Thus, the width of the inertial subrange narrows. It further proves the physical mechanism of the rotation effect, suppressing the horizontal development of plumes and reducing the energy dissipation.

Scaling laws for the second, fourth, and sixth order velocity and temperature structure functions are obtained in the inertial subrange, and closely agree with the theory proposed by

Chertkov [9] in the nonrotating system ($\Omega\tau = 0$). The scales satisfying the linear relationship for second, fourth, sixth order velocity and temperature structure functions gradually narrow with increasing $\Omega\tau$ at the same time. The spatial intermittency fluctuations of the velocity and temperature decrease with an increase of the Coriolis force.

The time evolution of the Kolmogorov dissipation scale $\eta(t)$, the kinetic-energy dissipation rate $\varepsilon_u(t)$, and the thermal dissipation rate $\varepsilon_\theta(t)$ will be studied along with the increase of $\Omega\tau$ in future work.

ACKNOWLEDGMENTS

This work was supported by the National Natural Science Foundation of China under Grants No. 11872337 and No.11902291. We also acknowledge the Joint Funds of the National Natural Science Foundation of China (Grant No. U1709209) and National Key R&D Program of China (Grant No. 2018YFB0204404), 2019 Program of Double Innovation, Jiangsu Province. We appreciate sincerely the referees's valuable comments on our work.

- [1] Q. Zhou, Y.-X. Huang, Z.-M. Lu, Y.-L. Liu, and R. Ni, Scale-to-scale energy and enstrophy transport in two-dimensional Rayleigh-Taylor turbulence, *J. Fluid Mech.* **786**, 294 (2016).
- [2] G. Boffetta, F. D. Lillo, A. Mazzino, and S. Musacchio, Bolgiano scale in confined Rayleigh-Taylor turbulence, *J. Fluid Mech.* **690**, 426 (2012).
- [3] A. G. W. Lawrie and S. B. Dalziel, Turbulent diffusion in tall tubes. I. models for Rayleigh-Taylor instability, *Phys. Fluids* **23**, 085109 (2011).
- [4] L. Biferale, F. Mantovani, M. Sbragaglia, A. Scagliarini, F. Toschi, and R. Tripiccion, High resolution numerical study of Rayleigh-Taylor turbulence using a thermal lattice Boltzmann scheme, *Phys. Fluids* **22**, 115112 (2010).
- [5] D. Lohse and K.-Q. Xia, Small-scale properties of turbulent Rayleigh-Bénard convection, *Annu. Rev. Fluid Mech.* **42**, 335 (2010).
- [6] G. Boffetta and A. Mazzino, Incompressible Rayleigh-Taylor turbulence, *Annu. Rev. Fluid Mech.* **49**, 119 (2017).
- [7] Q. Zhou, Temporal evolution and scaling of mixing in two-dimensional Rayleigh-Taylor turbulence, *Phys. Fluids* **25**, 036601 (2013).
- [8] G. Boffetta, A. Mazzino, S. Musacchio, and L. Vozella, Kolmogorov scaling and intermittency in Rayleigh-Taylor turbulence, *Phys. Rev. E* **79**, 065301(R) (2009).
- [9] M. Chertkov, Phenomenology of Rayleigh-Taylor Turbulence, *Phys. Rev. Lett.* **91**, 115001 (2003).

- [10] Y. Zhou, T. T. Clark, D. S. Clark, S. G. Glendinning, M. A. Skinner, C. M. Huntington, O. A. Hurricane, A. M. Dimits, and B. A. Remington, Turbulent mixing and transition criteria of flows induced by hydrodynamic instabilities, *Phys. Plasmas* **26**, 080901 (2019).
- [11] Y. Zhou, Rayleigh-Taylor and Richtmyer-Meshkov instability induced flow, turbulence, and mixing. I, *Phys. Rep.* **720**, 1 (2017).
- [12] Y. Zhou, Rayleigh-Taylor and Richtmyer-Meshkov instability induced flow, turbulence, and mixing. II, *Phys. Rep.* **723**, 1 (2017).
- [13] Y. Zhou, R. J. Williams, P. Ramaprabhu, M. Groom, B. Thornber, A. Hillier, W. Mostert, B. Rollin, S. Balachandar, P. Powell, A. Mahalov, and N. Attal, Rayleigh-Taylor and Richtmyer-Meshkov instabilities: A journey through scales, *Physica D* **423**, 132838 (2021).
- [14] Y. Zhou, W. H. Cabot, and B. Thornber, Asymptotic behavior of the mixed mass in Rayleigh-Taylor and Richtmyer-Meshkov instability induced flows, *Phys. Plasmas* **23**, 052712 (2016).
- [15] A. Baldwin, Kyle, M. Scase, Matthew, and J. Hill, Richard, The inhibition of the Rayleigh-Taylor instability by rotation, *Sci. Rep.* **5**, 11706 (2015).
- [16] G. Boffetta, A. Mazzino, and S. Musacchio, Rotating Rayleigh-Taylor turbulence, *Phys. Rev. Fluids* **1**, 054405 (2016).
- [17] T. Wei and D. Livescu, Late-time quadratic growth in single-mode Rayleigh-Taylor instability, *Phys. Rev. E* **86**, 046405 (2012).
- [18] O. Soulard and J. Griffond, Inertial-range anisotropy in Rayleigh-Taylor turbulence, *Phys. Fluids* **24**, 025101 (2012).
- [19] J.-J. Tao, X.-T. He, W.-H. Ye, and F. H. Busse, Nonlinear Rayleigh-Taylor instability of rotating inviscid fluids, *Phys. Rev. E: Stat., Nonlinear, Soft Matter Phys.* **87**, 013001 (2013).
- [20] G. F. Carnevale, P. Orlandi, Y. Zhou, and R. C. Kloosterziel, Rotational suppression of Rayleigh-Taylor instability, *J. Fluid Mech.* **457**, 181 (2002).
- [21] S. Chandrasekhar, *Hydrodynamic and Hydromagnetic Stability*, International Series of Monographs on Physics (Clarendon, Oxford, 1961).
- [22] Z.-L. Guo, B.-C. Shi, and C.-G. Zheng, A coupled lattice BGK model for the Boussinesq equations, *Int. J. Numer. Methods Fluids* **39**, 325 (2002).
- [23] Y.-H. Qian, D. d'Humières, and P. Lallemand, Lattice BGK models for Navier-Stokes equation, *Europhys. Lett.* **17**, 479 (1992).
- [24] Y.-H. Qian, Simulating thermohydrodynamics with lattice BGK models, *J. Sci. Comput.* **8**, 231 (1993).
- [25] C. K. Aidun, and J. R. Clausen, Lattice-Boltzmann method for complex flows, *Annu. Rev. Fluid Mech.* **42**, 439 (2010).
- [26] X.-W. Shan, Simulation of Rayleigh-Bénard convection using a lattice Boltzmann method, *Phys. Rev. E* **55**, 2780 (1997).
- [27] X.-Y. He, S.-Y. Chen, and D. Doolen, Gary, A novel thermal model for the lattice Boltzmann method in incompressible limit, *J. Comput. Phys.* **146**, 282 (1998).
- [28] X.-Y. Yang, H.-J. He, J. Xu, Y.-K. Wei, and H. Zhang, Entropy generation rates in two-dimensional Rayleigh-Taylor turbulence mixing, *Entropy* **20**, 738 (2018).
- [29] Y.-K. Wei, H.-S. Dou, Y.-H. Qian, and Z.-D. Wang, A novel two-dimensional coupled lattice Boltzmann model for incompressible flow in application of turbulence Rayleigh-Taylor instability, *Comput. Fluids* **156**, 97 (2017).
- [30] V. N. Goncharov, Analytical Model of Nonlinear, Single-Mode, Classical Rayleigh-Taylor Instability at Arbitrary Atwood Numbers, *Phys. Rev. Lett.* **88**, 134502 (2002).
- [31] M. J. Andrews, and D. B. Spalding, A simple experiment to investigate two-dimensional mixing by Rayleigh-Taylor instability, *Phys. Fluids* **2**, 922 (1990).
- [32] J. Griffond, B.-J. Gréa, and O. Soulard, Numerical investigation of self-similar unstably stratified homogeneous turbulence, *J. Turbul.* **16**, 167 (2015).
- [33] J. R. Ristorcelli and T. T. Clark, Rayleigh-Taylor turbulence: self-similar analysis and direct numerical simulations, *J. Fluid Mech.* **507**, 213 (2004).
- [34] N. Vladimirova and M. Chertkov, Self-similarity and universality in Rayleigh-Taylor, boussinesq turbulence, *Phys. Fluids* **21**, 015102 (2009).
- [35] G. Boffetta, A. Mazzino, S. Musacchio, and L. Vozella, Statistics of mixing in three-dimensional Rayleigh-Taylor turbulence at low Atwood number and Prandtl number one, *Phys. Fluids* **22**, 035109 (2010).
- [36] G. Boffetta, M. Magnani, and S. Musacchio, Suppression of Rayleigh-Taylor turbulence by time-periodic acceleration, *Phys. Rev. E* **99**, 033110 (2019).
- [37] G. Boffetta, F. D. Lillo, A. Mazzino, and L. Vozella, The ultimate state of thermal convection in Rayleigh-Taylor turbulence, *Physica D* **241**, 137 (2012).
- [38] S. Grossmann and D. Lohse, Scaling in thermal convection: A unifying theory, *J. Fluid Mech.* **407**, 27 (2000).